A Maximum NEC Criterion for Compton Collimation to Accurately Identify True Coincidences in PET

Garry Chinn and Craig S. Levin*, *Member, IEEE*

***Abstract*—In this work, we propose a new method to increase the accuracy of identifying true coincidence events for positron emission tomography (PET). This approach requires 3-D detectors with the ability to position each photon interaction in multi-interaction photon events. When multiple interactions occur in the detector, the incident direction of the photon can be estimated using the Compton scatter kinematics (Compton Collimation). If the difference between the estimated incident direction of the photon relative to a second, coincident photon lies within a certain angular range around colinearity, the line of response between the two photons is identified as a true coincidence and used for image reconstruction. We present an algorithm for choosing the incident photon direction window threshold that maximizes the noise equivalent counts of the PET system. For simulated data, the direction window removed 56%–67% of random coincidences while retaining $> 94\%$ of true coincidences from image reconstruction as well as accurately extracted 70% of true coincidences from multiple coincidences.**

***Index Terms*—Compton collimation, iterative image reconstruction, Monte Carlo simulation, multiple photon coincidences, noise equivalent counts (NEC), positron emission tomography (PET), random coincidences, 3-D positioning detector.**

I. Introduction

CADMIUM zinc telluride (CZT) can be used to build 3-D positioning positron emission tomography (PET) detectors with exceptional spatial and energy resolution [1]–[4]. However, CZT has relatively poor time resolution [1], [3]–[7] and low photoelectric fraction compared to scintillation detectors used in PET. Time resolution is important because coincidence detection [8] is used to form lines of response (LOR) for PET image reconstruction. The poor time resolution of CZT detectors lead to a relatively high rate of random coincidences and multiple coincidences [1], [3], [9] compared to scintillator-based detectors.

True coincident events (also called true events or trues) are associated with photon pairs produced by the same positron–electron annihilation event. Random LORs result from photon pairs produced by different positron–electron annihilation events. Random coincidences are background events that add noise and bias to the reconstructed image, degrading image contrast and quantitative accuracy. Multiple photon coincidences occur when more than two photons are recorded in the selected time window. In this case, for a standard PET system the true photon pairs cannot be identified and multiples are currently not used to reconstruct the image, effectively reducing the photon sensitivity of the system. High random and multiple photon rates will be a problem in any CZT system with high photon detection sensitivity.

For detectors with high 3-D spatial and energy resolution, the kinematics of Compton scatter within the detector can be used to electronically collimate photons (Compton collimation) [10]–[15]. In this work, we develop a classifier that uses Compton collimation to determine if a coincidence event is true or random. The use of Compton collimation for random rejection has previously been proposed [16], [17]. This method improves the accuracy of rejection of random events and can also identify true events when multiple photons are in coincidence. However, an optimal method for utilizing Compton collimation information has not been previously developed. In this work, we propose an algorithm that uses Compton collimation to maximize the noise equivalent counts of the system and provide simulation results to show the promise of this new framework compared to conventional coincidence detection.

II. Background

A. CZT Detectors

CZT is a wide bandgap, room temperature semiconductor that directly detects the charge produced by absorption of an ionizing particle. An example of a CZT detector design is shown in Fig. 1 [3] with anode and cathode cross strips sampling the interaction position along two dimensions. The position in the third dimension is computed from the anode-to-cathode signal ratio or the time difference between the cathode and anode time stamps [1], [2]. Uniform 1 mm $\times$ 1 mm $\times$ 1 mm spatial resolution can be achieved using 1 mm pitch anode and 5 mm cathode orthogonal cross strips [14]. The energy resolution has been measured at $\leq 2.5\%$ full-width half-maximum (FWHM) for 511 keV photons [1]. For CZT, the time resolution is on the order of 8 ns FWHM for 511 keV photopeak events. This time resolution is relatively poor compared to inorganic scintillators coupled to photodetectors [1]. These cross-strip CZT detectors are arranged in an edge-on configuration to provide high intrinsic photon detection efficiency and facilitate coupling to readout electronics. In CZT, the photo-fraction is roughly 19% versus $\sim 32\%$ in LSO. Thus, in both high-resolution CZT and

Manuscript received December 03, 2010; revised January 31, 2011; accepted January 31, 2011. Date of publication February 10, 2011; date of current version June 29, 2011. This work was supported in part by the U.S. National Institute of Health under Grant R01 CA120474, Grant R01 CA119056, Grant R01 CA119056-S1 (ARRA), and the Department of Energy under Grant DE SC0005290. *Asterisk indicates corresponding author.*

G. Chinn is with the Radiology Department, Stanford University, Stanford, CA 94305 USA (e-mail: gchinn@stanford.edu).

*C. S. Levin is with the Departments of Radiology, Physics, and Electrical Engineering, Stanford University, and the Molecular Imaging Program, Stanford, CA 94305 USA (e-mail: cslevin@stanford.edu).

Color versions of one or more of the figures in this paper are available online at http://ieeexplore.ieee.org.

Digital Object Identifier 10.1109/TMI.2011.2113379

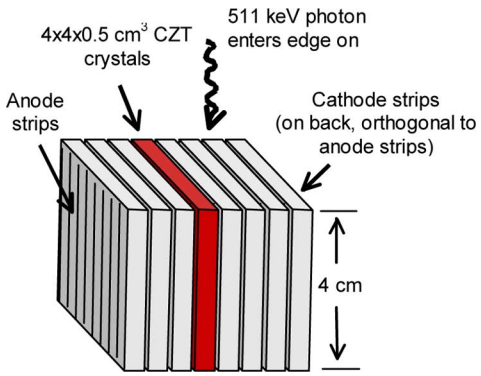

Fig. 1. Schematic of a 3-D positioning CZT detector with orthogonal cross-strip anodes and cathodes is shown. The detector is oriented edge-on to facilitate high photon detection efficiency since in this arrangement there is a minimum photon traversal path of 4 cm. The edge-on configuration also facilitates coupling to readout electronics. With 1 mm pitch anode and 5 mm cathode strips, the detector achieves 1 mm^3 spatial resolution with an energy resolution of 2.5% FWHM for 511 keV photons [1], [4].

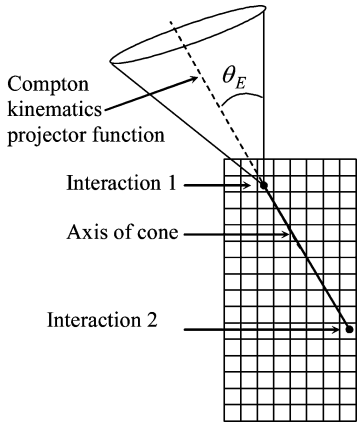

Fig. 2. Schematic of Compton kinematics is shown for the 3-D positioning CZT detector. The spatial location of two interactions in the detector determines the axis of the cone. The measured energy of the interactions determines the angle of the cone.

LSO detectors that employ small effective detector voxels, it is very likely that incoming 511 keV photons interact in more than one voxel element within the detector modules. Thus, in both cases (CZT and LSO) the energy window on each event is applied to the sum of all interactions per photon and not just on single interaction events. In the CZT detectors under study, we can position the individual coordinates of the multiple interactions, but in most high-resolution LSO designs, this cannot be done and only an effective energy weighted mean position is available. In CZT, if that sum energy of two or more interactions lies within roughly 6% around 511 keV, the event will be accepted. With a minimum photon material traversal distance of 4 cm, the intrinsic single 511 keV photon detection efficiency (including multiple interaction events that sum to a selected 5% window around the photopeak) is roughly 86% (74% for two photons in coincidence). With 3-D positioning capabilities, this detector can be used to reduce the parallax blurring effect [14] allowing the detectors to be positioned closer to the field of view for higher photon sensitivity than can be achieved by conventional 2-D positioning detectors [15]. Further, the high energy resolution improves the rejection of tissue-scattered photons that helps to reduce both scatter and random coincidence background for improved reconstructed image contrast [1], [3], [9]. In this work, we will investigate the utility of 3-D detectors that can position independent interactions within the detector for collimating incoming photons.

B. Photon Collimation by Compton Kinematics

With high 3-D spatial and energy resolution along with the capability to position individual interactions within the detector, the kinematics of Compton scatter in the detector can be used to electronically collimate photons [10]–[13]. Fig. 2 illustrates the process of *Compton collimation*. For 3-D PET detectors, Compton collimation can only be performed for 511 keV photons when the position and energy of the first two interactions in the detector are measured. Monte Carlo simulations suggest that 75% of all detected events involve one or more Compton interactions in CZT detectors [14]. A cone-surface projector function may be formed for the single photon event where the line formed by the two interactions form the cone axis and the cone half angle θ_E is calculated by

$$\cos\theta_E = 1 - m_e c^2 \left(\frac{1}{E_1} - \frac{1}{E_0}\right) \tag{1}$$

where E_0 is the incident photon energy and E_1 is the photon energy after the first Compton interaction deposits e_1 energy in the detector, m_e is the mass of an electron, and c is the speed of light. Doppler broadening, energy blurring and spatial blurring in the 3-D detector leads to angular blurring of the cone half-angle θ_E [13]. This is the Compton collimation angular resolution.

C. Clustering and Sequencing Interactions

In order to perform Compton collimation, the detector interactions must be spatially grouped (clustered), associated with an incoming photon, and sequenced. Compton interactions tend to scatter forward and given the good stopping power of CZT, the interactions produced from a single photon will generally be in close proximity to each other. The clustering problem becomes more difficult when multiple photons occur in the same or adjacent detectors. However, the probability that multiple photons are detected in close proximity is low and clustering errors can be considered a second-order effect.

The sequencing of interactions in 3-D detectors has previously been investigated [14]. For the energy and spatial resolution of CZT detectors, high-accuracy sequencing has been shown to be feasible. Pratx and Levin [14] showed that 78% sequencing accuracy was achievable for CZT detectors with 1 mm×5 mm×1 mm spatial resolution; higher accuracy is possible with $1 \times 1 \times 1$ mm^3 resolution.

III. Methods

A. Trues Classifier

In this section, we derive a classifier that will use Compton collimation to select true coincidences for image reconstruction. There are several possible categories for photon events: 1) trues, 2) single-scatter annihilation photon pairs, 3) multiscatter annihilation photon pairs, 4) single photons, and 5) scattered single

photons. Trues are detected photons produced from the same electron–positron annihilation event. Single-scatter annihilation pairs are detected photons produced from the same annihilation event with one and only one of the photons undergoing a single Compton scatter interaction within subject tissues. Multiscatter events have one or both annihilation photons in a coincidence pair undergo a total of at least two scatter interactions in the subject tissues. Single photons result when the photon cannot be paired in coincidence with another corresponding annihilation photon. Scattered single photons are single photons that have undergone scatter in tissue. We have previously shown that single-scatter annihilation photon pairs [18] and single photons [19] can be retained and not omitted from a dataset provided 3-D positioning detectors and an appropriate image reconstruction algorithm are used. However, these methodologies are unable to process multiscatter annihilation photon pairs and scattered single photons.

The trues classifier consists of an energy window, time window, and incident photon direction window from Compton collimation. An objective function is used to quantify the benefit of correctly identifying each of the event types and the cost for each type of classification error. The incident direction window parameters are then chosen to maximize this objective function. For this work, we will limit the objective function to trues and randoms. Unlike the conventional approach, the classifier can identify true annihilation photon pairs from multiple coincidences within the time window (as well as distinguish trues from randoms). Consequently, this classification problem can be solved using the framework of *multiple hypothesis testing* [20].

1) Energy Window: The classifier will make use of the conventional energy window [21]. The *energy window* is used to reject a high fraction of the photons that scattered in subject tissues before detection. If the total photon energy is outside the range $511 \pm e_c$ keV, where $e_c/511$ is the "energy resolution," the photon is assumed to have undergone one or more Compton scatter interactions within tissue and is rejected

2) Time Window: A time window [21] will also be used, but in a nonconventional way. In the conventional approach, a *time window* is used to select coincidence pairs of photons. When only a single photon or more than two photons appear in the window, the events are rejected. In our classifier, the time window is applied to create a set of photons called the *time neighborhood (set)* for each photon, which is used primarily to reduce the complexity of the search space. In our new method, true events may be found from any number of multiple coincident photons. If there are four or more photons in coincidence, two or more trues may be found.

For a time window of duration τ, the number of photons in one time neighborhood will be a Poisson distributed random number. Let H_T denote the hypothesis that a pair of detected photons were produced by the same positron–electron annihilation. The probability that a photon forms a true coincidence with another photon is given by the following conditional expectation:

$$P(H_T|k) = \frac{2E[k_T|k]}{k} \tag{2}$$

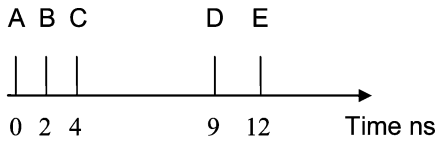

Photon	k	Neighbor photons
A	3	B, C
B	4	A, C, D
C	5	A, B, D, E
D	4	B, C, E
E	3	C, D

Fig. 3. An illustration of photons in a "time neighborhood." Photons A, B, C, D, and E are detected at 0, 2, 4, 9, and 12 ns, respectively. For time window $\tau = 8$ ns, the neighborhood size k and the neighboring photons is tabulated for each photon.

where k_T is the number of true coincidences in a time neighborhood with neighborhood size k, the number of photons in the neighborhood. Note that $2k_T \leq k$.

This *a priori* probability can be estimated by Monte Carlo simulation and will be used by the classifier. Note that this probability varies with the number of photons appearing in the time window.

An illustration of the time neighborhood is shown in Fig. 3. Five photons, labeled A–E, are shown recorded over a 12 ns time interval. For an 8 ns time window, the time neighborhood of photon A spans the time period from -8 ns to 8 ns and therefore includes photons B and C. The neighborhood size around A is $k = 3$. For photon C, the time neighborhood spans -4 ns to 12 ns and includes all shown photons, hence $k = 5$.

3) Incident Photon Direction Window: After energy and time windowing, an incident photon direction window is applied to determine true coincidences. Compton kinematics is used to estimate the direction of the incident photon. The line defined by the first two interactions will be referred to as the Compton cone axis and is shown in Fig. 4. The Compton scattering angle θ_E is determined by the measured energy of the first interaction using (1) and represents the direction of the incident photon relative to the Compton cone axis. Given any pair of detected photons, a LOR can be determined as the line through the detected positions. The angle between the LOR and the Compton cone axis is denoted by θ_P. The difference between these angles $\theta = |\theta_E - \theta_P|$ is a random variable due largely to the uncertainty of Compton collimation, which will be called the direction difference angle (DDA). Note that θ is centered around zero and is zero in the ideal noiseless case. The incident photon direction window is between 0° and an upper threshold. The photon pair is determined to be a true coincidence when the value of θ lies within this window.

If the LOR corresponds to a true coincidence, hypothesis H_T, the Gaussian distributed model

$$p_{H_T}(\theta) = \frac{2.3548}{F(2\pi)^{1/2}} e^{-2.773\theta^2/F^2} \tag{3}$$

is used, where F is the FHWM of the Compton collimation angular resolution of the detected photon. The Compton collimation angular resolution is dependent on the energy resolution,

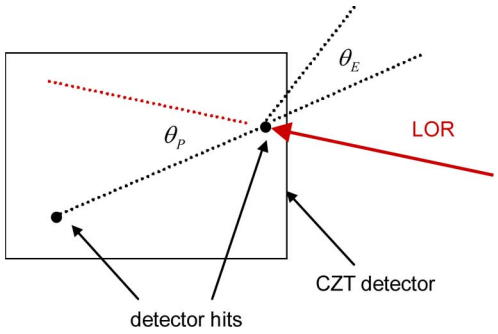

Fig. 4. Compton kinematics is used to calculate the expected angle between the LOR and the first two interactions in the detector. The line through the two detector hits defines the cone axis.

spatial resolution, and detector geometry. If the LOR is the result of two random photons in coincidence, hypothesis H_U, the distribution is modeled as a uniform distribution where

$$p_{H_U}(\theta) = \frac{1}{\pi}. \tag{4}$$

For k photons in the time neighborhood set, let the angle θ_i correspond to the direction difference angle for photon m and n_i, where $i = 1 \ldots k-1$ and with $L_i = (m, n_i)$ specifying the LOR between the detected position of the two photons. There are k possible hypotheses for photon m: either photon m and n_i are an annihilation pair (true or random) or photon m is a single photon.

A likelihood ratio [20] is used to test each hypothesis against an alternative. Let hypothesis H_i designate that photon m and n_i forms a true coincidence and when the classifier chooses this hypothesis, the decision rule D is

$$D = H_i : \begin{cases} \frac{p_{H_T}(\theta_i)}{p_{H_U}(\theta_i)} \geq \eta_1 \text{ and} \\ \frac{p_{H_T}(\theta_i)}{p_{H_T}(\theta_j)} \geq \frac{P(H_j|\theta_{E,j},\theta_{P,j})}{P(H_i|\theta_{E,i},\theta_{P,i})} \end{cases} \tag{5}$$

where $i, j = 1 \ldots k-1, \forall\, i \neq j$ and η_1 is a threshold.

The decision rule is simplified by assuming that the *a priori* probabilities $P(H_i|\theta_{E,i}, \theta_{P,i})$ are equal for all θ_i. If $\theta_i \geq \theta_0$ for $i = 1 \ldots k-1$, hypothesis H_U is the case where photon m is an unpaired photon. Since every photon n_i may have a different time neighborhood set from photon m, we must also test the time neighborhood sets of each photon η_i. Substituting (3) into the bottom of (5) yields

$$\begin{aligned} &\log \frac{2.3548}{(2\pi)^{1/2} F_i} - \frac{2.773\theta_i^2}{F_i} \\ &\quad \geq \log \frac{2.3548}{(2\pi)^{1/2} F_j} - \frac{2.773\theta_j^2}{F_j}\theta_i^2 \\ &\quad \leq \frac{F_i}{F_j}\theta_j^2 + \frac{1}{2.773}\left(\log \frac{2.3548}{(2\pi)^{1/2} F_i} - \log \frac{2.5348}{(2\pi)^{1/2} F_j}\right). \end{aligned}$$

Substituting (3) and (4) into the top of (5) and assuming that $F_i \cong F_j$, the decision rule of (5) simplifies to

$$D = H_i : \theta_i < \theta_0, \theta_i < \theta_j, \text{ and } \theta_i < \theta_{j,j'} \tag{6}$$

for every $j \neq i$ and for all j' in the time neighborhood of j. Hence, we have shown that the likelihood ratio test reduces to a simple incident photon direction window. The classification problem simplifies to the determination of the threshold value θ_0 for the direction window.

4) NEC Objective Function: In this work, thresholds are chosen to maximize the noise equivalent counts (NEC) [22]

$$\theta_0 = \arg\max\left(\frac{T^2}{T+S+R}\right) \tag{7}$$

where T is the number of trues (correctly identified annihilation photon pairs), R is the number of random photon pairs, and S is the number of scattered annihilation photon pairs. The NEC is detector figure-of-merit for a PET study's signal-to-noise ratio.

The true and random coincidence rates can be expressed as a function of the conditional decision probabilities. To review the notation, H_i denotes the hypothesis that the mth photon pairing with the ith photon is a true coincidence, H_T denotes the hypothesis that a true coincidence pair exists, and H_U denotes the hypothesis that the photon is unpaired. The decision can be D_U, an unpaired photon, or D_i, a true coincidence with the ith photon.

The true rate is given by

$$T = E\left[P(H_T)P(D_i|H_i)\right]. \tag{8}$$

A coincidence is true if $D_i|H_i$ or random if $D_{j\neq i}|H_i$. Therefore, we find that $P(D_i|H_i) + P(D_{j\neq i}|H_i) + P(D_U) = 1$ and the random rate can be calculated by

$$\begin{aligned} R &= E\left[P(H_T)P(D_{j\neq i}|H_i) + P(H_U)P(D_i|H_U)\right] \\ &= E\left[P(H_T)P(D_{j\neq i}|H_i)\right. \\ &\qquad \left. + (1 - P(H_T))\,(1 - P(D_s|H_U))\right] \\ &= E\left[P(H_T)\,(1 - P(D_i|H_i) - P(D_U|H_i))\right. \\ &\qquad \left. + (1 - P(H_T))\,(1 - P(D_U|H_U))\right] \end{aligned}$$

which simplifies to

$$\begin{aligned} R = E\left[P(H_T)\,(-P(D_i|H_i) - P(D_U|H_i)\right. \\ \left. + P(D_U|H_U)) + 1 - P(D_U|H_U)\right]. \end{aligned} \tag{9}$$

The decision probabilities are calculated as follows. For k photons in the time neighborhood, let the vector $\boldsymbol{\theta} = \theta_1 \ldots \theta_{k-1}$. Then the probability that the classifier correctly identifies the ith true coincidence is

$$P(D_i|H_i, \boldsymbol{\theta}) = P(|\theta_i| < \theta_0|H_i) \prod_{j\neq i} P(|\theta_i| < |\theta_j|\,|H_i\,, \theta_i)$$

where $\theta_i = \min_{j=1\ldots k}\{\theta_j\}$, so that

$$P(D_i|H_i, \boldsymbol{\theta}) = \int\limits_{|\theta|\leq\theta_o} p_{H_T}(\theta)d\theta \left(1 - \int\limits_{|\theta|\leq\theta_i} p_{H_U}(\theta)d\theta\right)^{k-2}$$

yielding

$$P(D_i|H_i,\boldsymbol{\theta}) = \frac{1}{2}\left(1+\operatorname{erf}\left(\frac{2.3548\theta_0}{\sqrt{2}F}\right)\right)\left(\frac{1-2\theta_i}{\pi}\right)^{k-2}. \quad (10)$$

Note that this decision probability is left as a conditional probability of the observed θ_i in order to simplify the calculation. Alternatively, the unconditional probability could have been calculated as

$$\begin{aligned}\prod_{j\neq i} P(|\theta_i| < |\theta_j|\,|H_i) &= \int_{\theta_i=0}^{\theta_0}\left(1-\int_{|\theta|\leq\theta_i} p_{H_U}(\theta)d\theta\right)^{k-2} d\theta_i \\ &= \frac{\pi}{2(k-1)}\left[\left(\frac{1-2\theta_0}{\pi}\right)^{k-1}-1\right]\end{aligned}$$

and then

$$P(D_i|H_i) = \frac{\pi}{2(k-1)}\left[\left(\frac{1-2\theta_0}{\pi}\right)^{k-1}-1\right]\frac{1}{2}\left(1+\operatorname{erf}\left(\frac{2.3548\theta_0}{\sqrt{2}F}\right)\right).$$

The probability of choosing D_s when the pairing with ith photon is a true coincidence is

$$P(D_U|H_i,\boldsymbol{\theta}) = \prod_{j\neq i} P(|\theta_j|>\theta_0|H_i)P(|\theta_i|>\theta_0|H_i)$$

$$P(D_U|H_i,\boldsymbol{\theta}) = \left(1-\int_{|\theta|\leq\theta_0} p_{H_U}(\theta)d\theta\right)^{k-2}\left[1-\int_{|\theta|\leq\theta_o} p_{H_T}(\theta)d\theta\right]$$

resulting in

$$P(D_U|H_i,\boldsymbol{\theta}) = \left(\frac{1-2\theta_0}{\pi}\right)^{k-2}\frac{1}{2}\left(1-\operatorname{erf}\left(\frac{2.3548\theta_0}{\sqrt{2}F}\right)\right). \quad (11)$$

Finally, the probability of classifying the photons as singles in the case of singles is

$$\begin{aligned}P(D_U|H_U,\boldsymbol{\theta}) &= \prod_j P(|\theta_j|>\theta_0|H_U) \\ &= \left(1-\int_{|\theta|\leq\theta_0} p_{H_U}(\theta)d\theta\right)^{k-1}\end{aligned}$$

yielding

$$P(D_U|H_U,\boldsymbol{\theta}) = \left(\frac{1-2\theta_0}{\pi}\right)^{k-1}. \quad (12)$$

Using (8)–(12), the true and random rates are reduced to

$$T(\boldsymbol{\theta}) = \frac{P(H_T|k)}{2}\left(\frac{1-2\theta_i}{\pi}\right)^{k-2}\left(1+\operatorname{erf}\left(\frac{2.3548\theta_0}{\sqrt{2}F}\right)\right) \quad (13)$$

and

$$\begin{aligned}R(\boldsymbol{\theta}) = P(H_T|k)\Bigg[&-\frac{1}{2}\left(\frac{1-2\theta_i}{\pi}\right)^{k-2}\left(1+\operatorname{erf}\left(\frac{2.3548\theta_0}{\sqrt{2}F}\right)\right) \\ &-\left(\frac{1-2\theta_0}{\pi}\right)^{k-2}\frac{1}{2}\left(1-\operatorname{erf}\left(\frac{2.3548\theta_0}{\sqrt{2}F}\right)\right) \\ &+\left(\frac{1-2\theta_0}{\pi}\right)^{k-1}\Bigg]-\left(\frac{1-2\theta_0}{\pi}\right)^{k-1}+1.\end{aligned} \quad (14)$$

Note that these rates are a function of the number of photons in the time neighborhood. Therefore, the thresholds will also vary depending on the number of photons in each time neighborhood. The computational cost of evaluating the objective function is low relative to the backprojection operation, so it is not critical to find a computationally efficient approach to find the incident photon direction threshold θ_0 that maximizes NEC over the interval $[0,\pi]$. A simple gradient ascent approach was used where the gradient of the NEC as a function of the angular threshold θ_0 is given by

$$\frac{d}{d\theta_0}\mathrm{NEC} = \frac{2T\frac{d}{d\theta_0}T\left(T+S+R\right)-T^2\left(\frac{d}{d\theta_0}T+\frac{d}{d\theta_0}R\right)}{\left(T+S+R\right)^2} \quad (15)$$

$$\frac{d}{d\theta_0}T = \frac{2.3548\sqrt{2}}{2\sqrt{\pi}F}P(H_T)\left(\frac{1-2\theta_i}{\pi}\right)^{k+k'-4}e^{-4\log(2)\theta_0^2/F^2} \quad (16)$$

$$\begin{aligned}\frac{d}{d\theta_0}R = P(H_T)\Bigg[&\frac{-2.3548\sqrt{2}}{2\sqrt{\pi}F}\left(\frac{1-2\theta_i}{\pi}\right)^{k+k'-4}e^{-4\log(2)\theta_0^2/F^2} \\ &-\frac{(k-2)}{\pi}\left(\frac{1-2\theta_0}{\pi}\right)^{k-3}\left(1-\operatorname{erf}\left(\frac{2.3548\theta_0}{\sqrt{2}F}\right)\right) \\ &+\frac{2.3548\sqrt{2}}{2\sqrt{\pi}F}\left(\frac{1-2\theta_0}{\pi}\right)^{k-2}e^{-4\log(2)\theta_0^2/F^2}\Bigg] \\ &-\frac{2(k-1)}{\pi}\left(\frac{1-2\theta_0}{\pi}\right)^{k-2}.\end{aligned} \quad (17)$$

5) Classification Algorithm: The decision rule (6) requires the comparison of the incident photon direction difference angles for all permutations of photon pairings. Because the decision rule is winner-takes-all, each comparison only needs to be computed once and stored.

For photon i, three variables are maintained: the time stamp t_i, smallest DDA θ_i', and index p_i of the photon that forms the smallest DDA. The photons are ordered by time stamp such that $t_i < t_{i+1}$. As previously defined, τ denotes the time window. Let $\theta_{i,j}'$ be the DDA for the LOR defined for photon i and j. The pseudo-code for the classifier is given as follows:

```
for all i
  for all j such that t_i < t_j + τ
    if θ'_{i,j} < θ'_i and θ'_{i,j} < θ'_j
      θ'_i = θ'_{i,j}
      θ'_j = θ'_{i,j}
      p_i = j
      p_j = i
for all i
  θ_0 = computeThreshold (i)
  if θ'_i < θ_0
      createLOREvent (i, p_i)
```

We profiled the computation time of the maximum NEC direction window (DW) and it was small ($< 2\%$) compared to the forward and backprojection operation. We used a small fixed step size for each iteration of the gradient ascent algorithm, which could be accelerated with a more intelligent selection of the step size that varies with each iteration. Also, most of the computations in the iterations could be replaced by faster lookup table operations, which would further accelerate the maximum NEC DW.

B. Monte Carlo Methods

CZT detectors that are capable of applying a direction window to incoming photons require many electronic readout channels and therefore are best suited for small FOV organ-specific PET [23], [24] such as a breast-dedicated camera or a small animal imaging system. Consequently, a dual-panel CZT PET system for breast imaging was selected as an example system to test these new processing algorithms. Note that the intent of this paper is to present and characterize the novel maximum NEC DW method, and not evaluate the design or performance of a dual-panel breast system, which has been studied elsewhere [25], [26]. This dual-panel system and its data collection for PET studies of the breast were simulated using a Monte Carlos simulation package developed in house, GRAY [27]. GRAY has been compared with GATE (Geant4) [28] and produced comparable singles and coincidence events for NEC calculations. Data was collected in list mode in order to apply the different algorithms in postprocessing. We simulated tissue-scattered events in the Monte Carlo experiments. The number of tissue-scattered events was small ($< 3\%$ of total counts for all simulated activity levels) given the limited volume between the panels and the fact that the narrow energy window removed most of tissue-scattered events that were present. Under these conditions, the performance of the breast imaging system could be improved by opening up the energy window. However, the goal of this study was to evaluate the ability of the maximum NEC DW method to reject randoms and extract trues from multiples. Therefore, we used the narrow energy window to focus on algorithm validation.

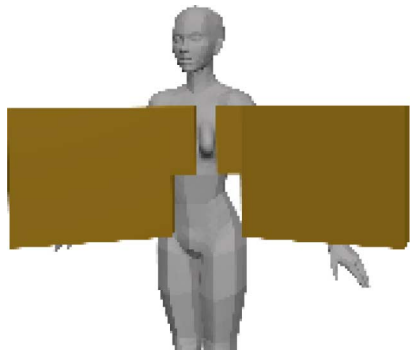

Fig. 5. Shown is an illustration of a simulated female patient with a dual-panel CZT PET system configured about one breast.

Each panel was 16 cm × 9.1 cm with a 2-cm-thick CZT detector similar to the one shown in Fig. 1. A schematic of the simulated female subject and two panels configured about her breast is shown in Fig. 5. To simulate the female subject a modified Fleur phantom was used [29]. This digital phantom uses uniform activity in the torso, head, and extremities with a hot spherical heart. A 5-mm-thick tungsten shield at the chest wall and 1.5-cm-thick shield at the top and bottom surround the detectors except at the opening to the front of the crystals. The shielding at the chest wall extends 5 mm in front of the crystals. This minimizes background counts emitted from the torso. The detectors were simulated with 1 mm × 1 mm × 1 mm intrinsic spatial resolution and a coincidence time resolution of 8 ns FWHM was simulated for CZT [2], [3]. The energy blur was simulated as Gaussian random noise sources with FWHM

$$\Delta e = \sqrt{6^2 + (0.022e)^2} \tag{18}$$

where e is the energy of the interaction in keV. This assumes that the readout electronics contributes a 6 keV FWHM white Gaussian noise source.

The angular resolution for Compton collimation was modeled by a simple Monte Carlo simulation. The angular resolution varies with the energy deposited by the first interaction. To model this dependence, the Compton scatter angle was calculated using (1) for E_1 varying from 490 to 170 keV in increments of 20 keV with noise added in accordance with (18). A Gaussian curve was fitted to the angular distribution produced from 100 000 trials.

The photon incident angle resolution achieved also depends on accurately determining the cone axis of the Compton collimation projector and is a function of the distance between the first two interactions. We estimated the angular resolution as a function of positioning uncertainty for the 3-D detector using a similar Monte Carlo simulation. This distance between the first two interactions was varied from 1 to 30 mm in increments of 1 mm with added positioning uncertainty in the form of a 3-D Gaussian noise function. A Gaussian curve was fitted to the distribution of the angular orientation of the cone axis produced from 100 000 trials. To calculate F, first described in (3), these two angular resolution components were added in quadrature.

As mentioned, a digital female phantom [29] with uniform activity in the body and a 4.5-cm-diameter spherical heart was

TABLE I
ACTIVITY IN THE ENTIRE PHANTOM, HEART, AND BREAST FOR THE SIMULATION STUDY

Phantom	Total Activity	Heart Activity	Breast Activity
A	1 mCi	0.043 mCi	.0033 mCi
B	5	0.215	.0165
C	10	0.43	.033
D	15	0.645	.0495
E	20	0.86	.066
F	30	1.29	.099

TABLE II
TYPICAL NUMBER OF SINGLES, AND TWO AND THREE-PHOTON COINCIDENCES AT EACH ACTIVITY LEVEL

Activity	Singles	Photon Pair Coincidences	Triple Photon Coincidences
1 mCi	8.5×10^6	2.3×10^5	3.9×10^2
5	4.2×10^7	1.4×10^6	1.1×10^4
10	8.4×10^7	3.3×10^6	4.9×10^4
15	1.2×10^8	5.8×10^6	1.2×10^5
20	1.7×10^8	8.8×10^6	2.2×10^5
30	2.4×10^8	1.6×10^7	5.5×10^5

used. The breast was compressed between the panels to 6 cm. Spherical lesions of 1.5 mm, 1.75 mm, 2.0 mm, and 3.0 mm diameter were placed in the breast with 10:1 sphere-to-background activity concentration consistent with FDG uptake in breast tumors [30]. In a practical breast imaging system, the total activity in the body is likely to be around 5 mCi. However, we simulated six different total activity levels from 1 to 30 mCi in order to create different ratios of trues, randoms, and multiples to study the sensitivity of our algorithm to these different operating conditions that may occur for different scanner geometries, for example. The activity in the heart and breast are shown in Table I. For each data set, 100-s acquisitions were simulated. The number of single, double, and triple coincidences within the time and energy window is shown in Table II.

The *a priori* true rate, (2), for each detector and LOR bin was estimated by Monte Carlo GRAY simulations of uniform phantoms without spherical activity foci. The estimated probabilities were rounded off to the nearest 0.01.

C. Methods for Identifying True Coincidences

We compared different methods for identifying true counts. For these cases, we used an 8 ns time window and a 498–524 keV energy window. A time window of the same duration as the FWHM coincidence time resolution was shown to optimize NEC [3], [15], [30].

1) Conventional method: The conventional coincidence method, using an energy and time window, served as a performance benchmark reference. When exactly two photons were detected within the selected energy and time windows, a LOR count was recorded for the detected positions. All other events were discarded.
2) Best fixed direction window: This method provides a "gold standard" reference for validating that our maximum NEC algorithm is correctly maximizing NEC. With Monte Carlo data, the identity of true and random events is known. For any given global threshold for the incident photon direction window, we use this information to calculate the true NEC of the system. This threshold was then manually adjusted by trial-and-error until the NEC was maximized for each Monte Carlo data set. Note that this method will not work with real data because the identity of true and random coincidences is not known and the true NEC cannot be calculated.
3) Maximum NEC DW: Our algorithm described in Section III-A was implemented with the Compton collimation angular resolution calculated by convolving the angular resolution as a function of energy with the angular resolution as a function of the distance between the first two interactions. Monte Carlo simulations were used to estimate these two functions. Using estimates of the angular resolution (described in Section III-B), the incident photon direction window threshold was calculated by maximizing (7) with the trues and random rates given by (13) and (14). Tissue-scatter events were modeled by a uniform distribution.

For varying phantom activity, we calculated the true and random rates from the Monte Carlo data. Using these rates, we calculated the NEC for the different methods.

IV. RESULTS

The performance of the maximum NEC DW will depend on the probability of randoms and true coincidences. To study the robustness of our algorithm to these probabilities, we varied the total activity in the phantom because the ratio of randoms and true will vary with activity. We studied a 10:1 activity concentration ratio between the hot spheres and background.

Fig. 6 shows an image reconstructed from a data set produced by the maximum NEC DW. The image was produced by an ordered subset list-mode maximum likelihood expectation maximization (OS ML-EM) algorithm [31]–[33] using 3 iterations of 10 subsets, which produced the best contrast-to-noise ratio results. We assumed that the true sequence of hits can be found accurately [14] and LORs were positioned on the first interaction. Rejecting random coincidences is not expected to yield any differences in resolution. For profiles drawn through the hot spheres, there was no significant difference in the resolution between the various methods.

Plots of the NEC, true, and random counts for the conventional, best fixed DW, and maximum NEC DW are shown in Figs. 7–9 for the six different activity levels. The best fixed DW is not a real method; it can only be implemented for Monte Carlo generated data when the identity of true coincidences is known. We use it simply as a gold standard to evaluate the effectiveness of our approach. The maximum NEC DW methodology significantly increased the NEC compared to the conventional approach largely by decreasing the number of random LORs. The maximum NEC DW and best fixed DW produced comparable results.

In Table III, a comparison of the NEC for the conventional, best fixed DW, and the maximum NEC DW are shown for six different activity levels in detail. There was no statistically significant difference between all three methods at 1 mCi activity. However, the maximum NEC DW yielded the best NEC for

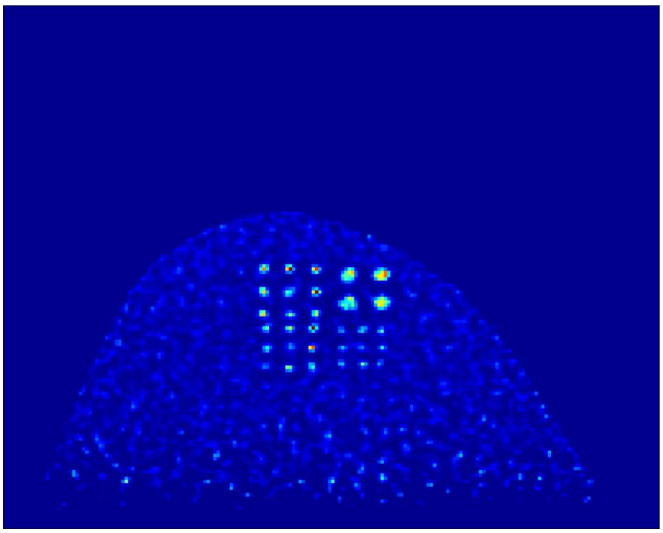

Fig. 6. Reconstructed image slice of the breast phantom parallel to the heads using three iterations, 10 subsets of the 3-D OS-EM algorithm for a 10 mCi total body dose for data processed using the maximum NEC direction window. The simulated data corresponds to 100 s of acquisition time in the high sensitivity dual-panel breast system. Spherical lesions of 1.5 mm, 1.75 mm, 2.0 mm, and 3.0 mm diameter were placed in the breast with 10:1 sphere-to-background activity concentration ratio.

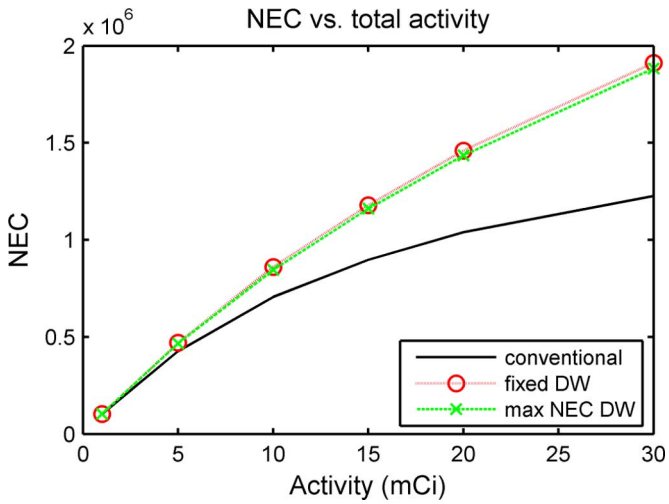

Fig. 7. NEC versus total activity for different windowing methods. Only a PET system with 3-D positioning detectors can select an incident photon direction window (DW).

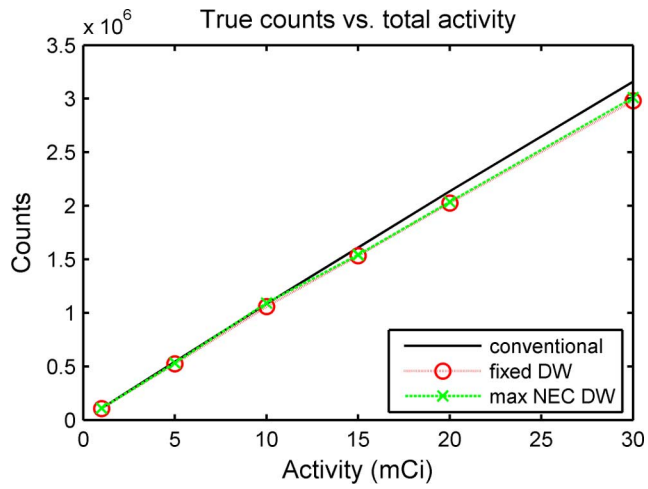

Fig. 8. Plot of true counts versus total activity for different windowing methods.

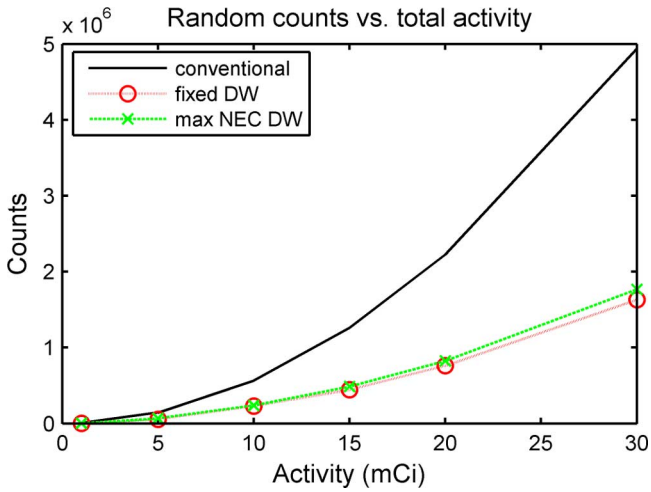

Fig. 9. Plot of random counts versus total activity for different windowing methods.

TABLE III
COMPARISON OF NEC FOR CONVENTIONAL TIME WINDOW VERSUS OPTIMIZED FIXED THRESHOLD DIRECTION WINDOW, AND MAXIMUM NEC ALGORITHM USING A GLOBAL THRESHOLD. FOR THE FIXED WINDOW, THE WINDOW THRESHOLD IN RADIANS IS SHOWN IN PARENTHESES

Phan. mCi	Conventional ($x10^3$)	Best Fixed DW ($x10^3$)	Max NEC DW ($x10^3$)
1	102.7±0.3	103.6±0.3	102.9±0.3
5	426.5±0.7	466.3±0.7	469.5±0.7
10	706.2±0.8	845.2±0.9	860.9±0.9
15	897.0±0.9	1160.9±1.1	1178.8±1.1
20	1039.5±1.0	1435.0±1.2	1459.8±1.2
30	1226.1±1.1	1882.4±1.4	1911.4±1.4

5–30 mCi. The improvement was statistically significant compared to the conventional method and varied from 10% at 5 mCi to 56% at 30 mCi. For all activities there was a small ($< 2\%$ across all activity levels) difference between results for the maximum NEC DW and the best fixed DW. The maximum NEC DW generally outperformed the best fixed DW (except at 1 mCi activity) because it does not use one global value for the window. The maximum NEC DW can adapt the window to the variable Compton collimation blur due to nonconstant energy resolution and uncertainty of the cone axis direction.

Tables IV and V show, respectively, the number of true and random counts for the conventional, best fixed DW, and maximum NEC DW methods. The maximum NEC DW removed between 2.5% of the true counts at 1 mCi to 6% of the true counts at 30 mCi. However, the random counts were reduced by 56% at 1 mCi, 62% at 5 mCi, and 64%–67% at 10–30 mCi. There was a small difference between the maximum NEC DW and the best fixed DW for trues (1%) and larger for randoms (approximately 10% for most activity levels).

Table VI shows the tissue-scatter events for the conventional, best fixed DW, and maximum NEC DW methods. Both the best fixed DW and maximum NEC DW method rejects scatter

TABLE IV
NUMBER OF TRUE EVENTS BY METHOD IS SHOWN

Phan. mCi	Conventional ($x10^3$)	Best Fixed DW ($x10^3$)	Max NEC DW ($x10^3$)
1	109.4±0.3	108.6±0.3	106.7±0.3
5	544.0±0.7	530.8±0.7	525.1±0.7
10	1081.2±1.0	1092.1±1.0	1059.5±1.0
15	1610.6±1.3	1541.8±1.2	1535.2±1.2
20	2136.0±1.5	2035.9±1.4	2026.8±.1.4
30	3158.7±1.8	3010.7±1.7	2981.3±.1.7

TABLE V
NUMBER OF RANDOM LORS BY METHOD IS SHOWN

Phan. mCi	Conventional ($x10^3$)	Best Fixed DW ($x10^3$)	Max NEC DW ($x10^3$)
1	5.7±0.1	3.8±0.1	2.5±0.1
5	142.6±0.4	66.4±0.3	55.1±0.2
10	564.8±0.7	230.3±0.5	224.6±0.5
15	1260.5±1.1	486.0±0.7	444.3±0.7
20	2225.0±1.5	825.7±0.9	759.7±0.9
30	4937.1±2.2	1765.6±1.3	1630.0±1.3

TABLE VI
NUMBER OF SCATTER EVENTS BY METHOD IS SHOWN

Phan. mCi	Conventional ($x10^3$)	Best Fixed DW ($x10^3$)	Max NEC DW ($x10^3$)
1	1.45±0.1	1.44±0.1	1.42±0.1
5	7.2±0.1	7.02±0.1	6.95±0.1
10	14.0±0.2	13.4±0.1	13.6±0.1
15	20.8±0.2	19.9±0.2	19.8±0.2
20	28.0±0.3	26.5±0.2	26.4±0.2
30	41.4±0.4	38.8±0.3	38.5±0.3

events less efficiently than they reject random coincidences. This result is not surprising because tissue-scatter events were negligible in these simulations. For example, at 5 mCi, true events outnumbered tissue-scatter events by approximately 75 to 1 and random coincidences outnumbered tissue-scatter events by 20 to 1. Therefore, the best NEC will be achieved by choosing a direction window threshold that mitigates random coincidences over tissue-scatter events. It is more important to note that the maximum NEC DW continues to match or exceed the gold standard best fixed DW for both random coincidence and tissue-scatter event rejection.

The maximum NEC DW was also effective at extracting true photon pairs from multiple coincidences with a low fraction of random events as shown in Fig. 10. Approximately 70% of the true photon pairs were correctly identified from multiples (accuracy is known from Monte Carlo list mode data). In other words, the type I error rate was approximately 30% (the fraction of trues identified as randoms). Of the counts selected from multiple coincidences, the type II error rate was only 20%–30%; the fraction of accepted events that were randoms. For three photons in coincidence, there are three possible pairings and at most only one correct pairing. If photons were paired randomly, the type II error rate would be greater than 66%, so our maximum NEC DW method is performing significantly better than random assignment.

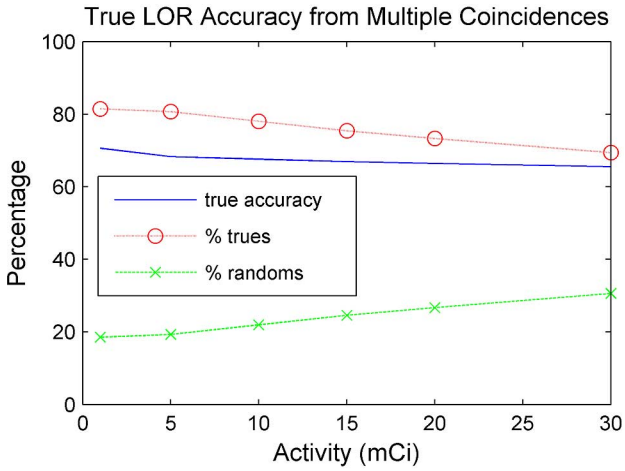

Fig. 10. Summary of maximum NEC incident photon direction window extraction of true counts from multiple coincidence events. The percentage of the accepted counts that were true are shown with red open circles over a dotted line. The percentage of the accepted counts that were random are shown with the green dashed lines for 1–30 mCi activity. Of the counts accepted by the direction window, 70%–80% were true counts. The true accuracy is the percentage of true counts that were successfully identified where 100% true accuracy results if all the true counts in the data are accepted by the direction window. The true accuracy, shown as a solid blue line, was approximately 70% for 1–30 mCi activity. The direction window rejects 30% of the potential true counts in multiple coincidences. Using random assignment, forming coincidence events from three photon coincidences would yield 33% of accepted counts as true counts with a true accuracy of 33%.

V. DISCUSSION AND CONCLUSION

The work presented here demonstrates a new framework for using 3-D positioning detectors to produce additional information that can reduce the number of random coincidences and identify true from multiple coincidences. The scope of this work was to demonstrate the proof of principle of a new algorithm for identifying true coincidences for PET imaging. This technique can compensate for the poor randoms rejection capabilities due to limited time resolution of CZT detectors. It can also recover a high fraction of trues from multiple coincidences instead of rejecting these events as is done by the current approaches. While current systems have low absolute photon sensitivity ($< 10\%$), future systems, especially small animal systems may employ higher geometrical and detection efficiencies [15]. The current study focused on data from a dual-panel system geometry. Further investigations are underway to determine whether a system with higher absolute photon sensitivity (e.g., $> 15\%$) will benefit even more from the proposed methods to utilize rather than reject multiple (> 2) photon coincidence events.

The improvement on NEC by the incident photon direction window technique we have introduced in this paper should not depend on the distribution of the activity (e.g., activity concentration ratios) but, rather on the absolute rates of multiples and/or randoms. That is, using incident photon angle information, this approach helps to increase good counts by extracting trues from normally discarded multiples, and decrease background, by rejecting randoms. The observed improvements in NEC shown in Fig. 7 and Table III should correlate well with $(\mathrm{SNR})^2$ [34]. Thus, it is expected that this method is most effective for systems with high randoms or multiple coincidence rates, which is not necessarily the case for the dual-panel breast

system studied (see Fig. 5) since the breast activity is relatively small (see Table I) and the detectors can be well shielded from background activity.

CZT PET systems for small animal, prostate, or cardiac imaging can have both high random and multiple coincidence rates due to effects such as very high solid angle coverage inadequate shielding from background activity, and/or high activity in the field of view. Further work is needed to investigate applications that could benefit the most from the direction window methodology studied in this paper.

In conventional PET, the time window is used as a first pass to filter randoms and multiples. Our approach uses a combination of the time window and the direction window to perform a first pass filtering of randoms and multiples. Therefore, the direction window does not replace random correction approaches such as delayed coincidence [35] or singles calculation [36], which can still be applied to further mitigate randoms. Randoms correction algorithms remove the bias introduced by random coincidences but, add noise that is proportional to the random coincidence rate. The direction window will therefore reduce the amount of noise added by the random coincidence correction by reducing the random coincidence rate before correction is applied. Note that the efficiency of extracting true photon pairs from multiples is fairly constant as a function of activity (Fig. 10).

Further work is needed to fully characterize this new algorithm as a function of Compton collimation angular resolution. In this study, we assumed that the sequence of multi-interaction detector events was known. Inaccurate sequencing will reduce the performance of the incident photon direction window. The accuracy of the sequencing algorithm is dependent on the Compton collimation angular resolution. For a solid $1 \times 5 \times 1$ mm^3 CZT detector with 2.5% energy resolution at 511 keV, a maximum a posteriori (MAP) sequencing algorithm was shown to be 78% accurate [14]. For perfect angular resolution, the MAP sequencing algorithm would be nearly 100% accurate and the maximum NEC DW method would reject nearly 100% of all random and scatter events while retaining nearly 100% of the true coincidences, which is also the case with perfect time resolution.

Detectors could be designed to improve the performance of the sequencing algorithm and max NEC DW methods. It has been shown that the angular resolution improves with increasing distance between the first two interactions [13]. At interaction distances below 5 mm, the angular resolution is so poor that the sequencing algorithm is likely to be highly inaccurate and the direction window is so wide that it is ineffective at filtering randoms. A layered PET detector geometry, with multiple separated detector sections, such as that used in a Compton camera, would increase the average distance between interactions, improving sequencing accuracy and the direction window method performance. There are also efforts to develop submillimeter CZT detectors [37]–[39] that would also improve the angular resolution.

Improving the detector design to improve Compton collimation angular resolution would likely yield the largest improvement to the performance of the maximum NEC DW method. However, there are also some algorithmic improvements that may be explored. The incident photon direction window algorithm investigated in this study could also be improved in several ways. First, the 8 ns coincidence time window was chosen to optimize the performance of the conventional coincidence window method. Worse coincidence time resolution or a different time window might have improved the relative performance of the maximum NEC DW. Second, we did not implement the double Compton collimation case (see Appendix). When Compton collimation can be performed on both detected photons, a 2-D direction window can be applied that more accurately identify trues and randoms. This will improve the accuracy of rejecting randoms and the extraction of trues from multiples. Compton collimation was shown to be available for a detected photon approximately 75% of the time in CZT detectors [14]. Therefore, double Compton collimation is expected to be available 56% of the time. Third, we used simplified PDF and *a priori* models. More accurate models would also improve the performance of the algorithm while incurring higher computational cost. Fourth, the accuracy of the scatter distribution model included in the maximum NEC objective function can be improved. The tissue scatter rate S is not dependent on θ_0 and can be estimated using a Monte Carlo technique or another scatter estimation technique [40], [41]. Further, a wider energy window could have been used with the maximum NEC DW used to reject tissue-scattered coincidences. Opening a wider energy window will increase the number of counts, which will improve the NEC if scatter events can be accurately identified and rejected. Fifth, a randoms correction algorithm should be applied to remove the bias caused by the residual randoms after direction windowing. The existing randoms correction algorithms could be adapted. To assess the practical performance of our new approach, the maximum NEC DW after randoms correction should be compared against the conventional approach after randoms correction. Finally, in this work we investigated using NEC as the objective function. While NEC is easily calculated, absolute quantitation of the reconstructed images is an equally important metric. Other more effective objective functions might exist that could be implemented following the framework presented here.

In conclusion, we introduced an incident photon direction window for systems that use 3-D positioning detectors that can effectively be used to remove random LORs and recover true LORs from multiple coincidence events. Our proof of principle demonstration shows that the maximum NEC DW method is a promising approach that can compensate for the poor time resolution of CZT detectors. However, further work is necessary. As we have discussed, there are many different methods for further improvements to the methods. Also, there is a need to fully characterize the algorithm and to identify the system designs, detector designs, and applications that can benefit the most from this new methodology.

APPENDIX

In the case when Compton scatter collimation is available for both detected photons, the incident photon direction window becomes 2-D. We will call this the double Compton collimation case. For this study, we did not implement the double Compton collimation case. However, we provide the derivation here for completeness. Let θ_1 and θ_2 denote the direction difference angles at the first and second detectors for the respective photons

in a pair. Then the probability density functions under the annihilation pair and singles hypotheses are given by

$$p_{H_T}(\theta_1,\theta_2)=\frac{2.3548^2}{2\pi F_1F_2}e^{-2.773\theta_1^2/F_1^2-2.773\theta_2^2/F_2^2} \tag{19}$$

where F_i is the angular FWHM at the ith detector and

$$p_{H_s}(\theta_1,\theta_2)=\frac{1}{\pi^2}. \tag{20}$$

Using a similar derivation to (6), the decision rule then becomes

$$D=H_i:\theta_{i,1}+\theta_{i,2}<\phi_0 \text{ and } \theta_{i,1}+\theta_{i,2}<\theta_{j,1}+\theta_{j,2} \tag{21}$$

where $\theta_{i,1}$ and $\theta_{i,2}$ are the DDA for photon 1 and 2, respectively.

To calculate the NEC and its derivative, we use the decision probabilities $P(D_i|H_i,\boldsymbol{\theta})$, $P(D_U|H_i,\boldsymbol{\theta})$, and $P(D_U|H_U,\boldsymbol{\theta})$ for the observed $\boldsymbol{\theta}=\theta_1\ldots\theta_{k-1}$.

$$P(D_i|H_i,\boldsymbol{\theta})=\prod_{j\neq i}P(|\theta_{i,1}+\theta_{i,2}|<|\theta_{j,1}+\theta_{j,2}|\big|H_i)P(R_i|H_i)$$

where $R_i=\{|\theta_{i,1}+\theta_{i,2}|<\phi_0\}$ and $\phi_i=\min_{j=l\cdot k}\{\theta_{j,1}+\theta_{j,2}\}$.

Using

$$\begin{aligned}\prod_{j\neq i}&P(|\theta_{i,1}+\theta_{i,2}|<|\theta_{j,1}+\theta_{j,2}|\,|H_i)\\&=\left(1-4\int_0^{\theta_1}\int_0^{\phi_i-\theta_1}p_{H_U}(\theta_1,\theta_2)d\theta_2d\theta_1\right)^{k-2}\\&=\left(1-\frac{2\phi^2}{\pi^2}\right)^{k-2}\end{aligned}$$

and

$$P(R_i|H_i)=4\int_0^{\phi_0}\int_0^{\phi_0-\theta_1}p_{H_T}(\theta_{i,1},\theta_{i,2})d\theta_2d\theta_1.$$

yields

$$\begin{aligned}&P(D_i|H_i,\boldsymbol{\theta})\\&\quad=4\left(1-\frac{2\phi^2}{\pi^2}\right)^{k-2}\int_0^{\phi_0}\int_0^{\phi_0-\theta_1}p_{H_T}(\theta_{i,1},\theta_{i,2})d\theta_2d\theta_1.\end{aligned} \tag{22}$$

Next

$$P(D_U|H_i,\boldsymbol{\theta})=\prod_{j\neq i}P(\phi_0<|\theta_{j,1}+\theta_{j,2}|)P\left(R_i^C|H_i\right)$$

and because

$$\begin{aligned}\prod_{j\neq i}&P(\phi_0<|\theta_{j,1}+\theta_{j,2}|)\\&=\left(1-4\int_0^{\phi_0}\int_0^{\phi_0-\theta_1}p_{H_U}(\theta_{i,1},\theta_{i,2})d\theta_2d\theta_1\right)^{k-2}\\&=\left(1-\frac{2\phi_0^2}{\pi^2}\right)^{k-2}\end{aligned}$$

then

$$\begin{aligned}P(D_U|H_i,\boldsymbol{\theta})=&\left(1-\frac{\phi_0^2}{2\pi^2}\right)^{k-2}\\&\left[1-4\int_0^{\phi_0}\int_0^{\phi_0-\theta_1}p_{H_T}(\theta_{i,1},\theta_{i,2})d\theta_2d\theta_1\right].\end{aligned} \tag{23}$$

Finally,

$$\begin{aligned}&P(D_U|H_U,\boldsymbol{\theta})\\&\quad=\prod_iP(\phi_0<|\theta_{j,1}+\theta_{j,2}|)\\&\quad=\left(1-4\int_0^{\phi_0}\int_0^{\phi_0-\theta_1}p_{H_U}(\theta_{i,1},\theta_{i,2})d\theta_2d\theta_1\right)^{k-1}\end{aligned}$$

which yields

$$P(D_U|H_U,\boldsymbol{\theta})=\left(1-\frac{2\phi_0^2}{\pi^2}\right)^{k-1}. \tag{24}$$

(21)–(23) can then be substituted into (8) and (9) to derive the true and random coincidence rates for the NEC calculation.

ACKNOWLEDGMENT

The authors would like to thank P. D. Olcott for the use of GRAY for Monte Carlo simulations.

REFERENCES

[1] C. S. Levin, "New imaging technologies to enhance the molecular imaging sensitivity of positron emission tomography," *Proc. IEEE*, vol. 96, no. 3, pp. 439–467, Mar. 2008.

[2] C. S. Levin, J. L. Mattesson, R. T. Skelton, F. Duttweiler, G. Huszar, and P. C. LeBlanc, "Promising characteristics and performance of cadmium zinc telluride for positron emission tomography. 2004 nuclear science symposium and medical imaging conference," in *IEEE Nucl. Plasma Sci. Soc.*, Rome, Italy, 2004, pp. 136–136, Abstract # M2-117, Book of Abstracts.

[3] C. S. Levin, A. M. K. Foudray, and F. Habte, "Impact of high energy resolution detectors on the performance of a PET system dedicated to breast cancer imaging," *Physica Medica*, vol. 21, pp. 28–34, 2006.

[4] Y. Gu, J. L. Matteson, R. T. Skelton, A. C. Deal, E. A. Stephan, F. Duttweiler, T. M. Gasaway, and C. S. Levin, "Study of a high resolution, 3-D positioning cross-strip cadmium zinc telluride detector for PET," in *Phys. Med. Bio.*, 2011, pp. 1563–1584.

[5] Y. Okada, T. Takahashi, G. Sato, S. Watanabe, S. Nakazawa, K. Mori, and K. Makishima, "CdTe and CdZnTe detectors for timing measurements," in *IEEE Nuc. Sci. Symp. Med. Imag. Conf. Rec.*, 2001, pp. 2429–2433.

[6] E. Bertolucci, M. Conti, C. A. Curto, and P. Russo, "Timing properties of CdZnTe detectors for positron emission tomography," *Nuc. Instrum. Methods Phys. Res. A*, vol. 400, no. 1, pp. 107–112, 1997.

[7] L. Meng and Z. He, "Exploring the limiting timing resolution for large volume CZT detectors with waveform analysis," *Nuc. Instrum. Methods A*, vol. 550, pp. 435–445, 2005.

[8] M. E. Phelp, E. J. Hoffman, N. A. Mullani, and M. M. Ter-Pogossian, "Application of annihilation coincidence detection to transaxial reconstruction tomography," *J. Nucl. Med.*, vol. 16, no. 3, pp. 210–224, 1975.

[9] C. S. Levin and H. Zaidi, "Current trends in preclinical PET system design," *PET Clinics*, vol. 2, no. 2, pp. 125–160, 2007.

[10] D. B. Everett, J. S. Fleming, R. W. Todd, and J. M. Nightingale, "Gamma-radiation imaging system based on the Compton effect," *Proc. IEE*, vol. 124, pp. 995–1000, 1977.

[11] M. Singh, "An electronically collimated gamma camera for single photon emission computed tomography, part I: Theoretical considerations and design criteria," *Med. Phys.*, vol. 10, pp. 421–427, 1983.

[12] M. Singh and D. Doria, "An electronically collimated gamma camera for single photon emission computed tomography, part II: Image reconstruction and preliminary experimental measurements," *Med. Phys.*, vol. 10, pp. 428–435, 1983.

[13] Y. F. Du, Z. He, G. F. Knoll, D. K. Wehe, and W. Li, "Evaluation of a Compton scattering camera using 3-D position sensitive CdZnTe detectors," *Nuc. Instr. Methods Phys. Res. A*, vol. 457, pp. 203–211, 2001.

[14] G. Pratx and C. S. Levin, "Bayesian reconstruction of photon interaction sequences for high-resolution PET detectors," *Phys. Med. Bio.*, vol. 54, pp. 5073–5094, 2009.

[15] F. Habte, A. M. K. Foudray, P. D. Olcott, and C. S. Levin, "Effects of system geometry and other physical factors on photon sensitivity of high-resolution positron emission tomography," *Phys. Med. Bio.*, vol. 52, pp. 3753–3772, 2007.

[16] J. E. Gillam, T. E. Beveridge, and R. A. Lewis, "Positron emission imaging using acquired cone-surfaces from opposing Compton cameras," in *IEEE Nuc. Sci. Symp. Conf. Rec.*, 2004, pp. 2810–2814.

[17] S.-J. Park, W. L. Rogers, and N. H. Clinthorne, "Improvement of noise equivalent count rate using Compton kinematics in a Compton PET," *IEEE Trans. Nucl. Sci.*, vol. 54, no. 5, pp. 1589–1598, Oct. 2007.

[18] G. Chinn, A. M. K. Foudray, and C. S. Levin, "Accurately positioning and incorporating tissue-scattered photons into PET image reconstruction," in *IEEE Nucl. Sci. Symp. Conf. Rec.*, Oct. 2006, vol. 3, pp. 1746–1751.

[19] G. Chinn, A. M. K. Foudray, and C. S. Levin, "A method to include single photon events in image reconstruction for a 1 mm resolution PET system built with advanced 3-D positioning detectors," in *IEEE Nucl. Sci. Symp. Conf. Rec.*, 2006, pp. 1740–1745.

[20] A. D. Whalen, *Detection of Signals in Noise*. San Diego, CA: Academic, 1971.

[21] S. R. Cherry, J. A. Sorenson, and M. E. Phelps, *Physics in Nuclear Medicine*. Philadelphia, PA: Elsevier, 2003.

[22] S. C. Strother, M. E. Casey, and E. J. Hoffman, "Measuring PET scanner sensitivity: Relating countrates to image signal-to-noise ratios using noise equivalent counts," *IEEE Trans. Nucl. Sci.*, vol. 37, no. 2, pp. 783–788, Apr. 1990.

[23] C. S. Levin, "Detector design issues for compact nuclear emission cameras dedicated to functional breast imaging," *Nucl. Instrum. Methods Phys. Res.*, vol. 497, no. 1, pp. 60–74, 2003.

[24] C. S. Levin, A. M. K. Foudray, and F. Habte, "Impact of high energy resolution detectors on the performance of a PET system dedicated to breast cancer imaging," *Physica Medica*, vol. 21, pp. 28–34, 2006.

[25] J. Zhang, P. D. Olcott, G. Chinn, A. M. K. Foudray, and C. S. Levin, "Study of the performance of a novel 1 mm resolution dual-panel PET camera design dedicated to breast cancer imaging using Monte Carlo simulation," *Med. Phys.*, vol. 34, pp. 689–702, 2007.

[26] H. Peng and C. S. Levin, "Design study of a high-resolution breast-dedicated PET system built from cadmium zinc telluride detectors," in *Phys. Med. Biol.*, 2010, vol. 55, pp. 2761–2788.

[27] P. D. Olcott, S. R. Buss, C. S. Levin, G. Pratx, and C. K. Sramek, "GRAY: High energy photon ray tracer for PET applications," in *IEEE Nucl. Sci. Symp. Conf. Rec.*, 2006, pp. 2011–2015.

[28] S. Jan, G. Santin, D. Strul, S. Staelens, K. Assié, D. Autret, S. Avner, R. Barbier, M. Bardiès, P. M. Bloomfield, D. Brasse, V. Breton, P. Bruyndonckx, I. Buvat, A. F. Chatziioannou, Y. Choi, Y. H. Chung, C. Comtat, D. Donnarieix, L. Ferrer, S. J. Glick, C. J. Groiselle, D. Guez, P. F. Honore, S. Kerhoas-Cavata, A. S. Kirov, V. Kohli, M. Koole, M. Krieguer, D. J. van der Laan, F. Lamare, G. Largeron, C. Lartizien, D. Lazaro, M. C. Maas, L. Maigne, F. Mayet, F. Melot, C. Merheb, E. Pennacchio, J. Perez, U. Pietrzyk, F. R. Rannou, M. Rey, D. R. Schaart, C. R. Schmidtlein, L. Simon, T. Y. Song, J. M. Vieira, D. Visvikis, R. Van de Walle, E. Wieërs, and C. Morel, "GATE: A simulation toolkit for PET and SPECT," *Phys. Med. Biol.*, vol. 49, pp. 4543–4561, 2004.

[29] P. D. Olcott, F. W. Y. Lau, and C. S. Levin, "Data acquisition system design for a 1 mm3 resolution PSAPD-based PET system," in *IEEE Nucl. Sci. and Med. Imag. Conf. Rec.*, 2007, pp. 3206–3211.

[30] J. Zhang, P. D. Olcott, G. Chinn, A. M. K. Foudray, and C. S. Levin, "Study of the performance of a novel 1 mm resolution dual-panel PET camera design dedicated to breast cancer imaging using Monte Carlo simulation," *Med. Phys.*, vol. 34, no. 2, pp. 689–702, 2007.

[31] L. A. Shepp and Y. Vardi, "Maximum likelihood reconstruction for emission tomography," *IEEE Trans. Med. Imag.*, vol. 1, no. 2, pp. 113–122, 1982.

[32] L. Parra and H. H. Barrett, "List mode likelihood: EM algorithm and image quality estimation demonstrated on 2-D PET," *IEEE Trans. Med. Imag.*, vol. 17, no. 2, pp. 228–235, Apr. 1998.

[33] H. M. Hudson and R. S. Larkin, "Accelerated image reconstruction using ordered subsets of projected data," *IEEE Trans. Med. Imag.*, vol. 13, no. 4, pp. 601–609, Dec. 1994.

[34] C. W. Stearns, "NEC and local image noise in PET imaging," in *IEEE Nucl. Sci. Symp. Conf. Rec.*, 2004, pp. 3106–3108.

[35] M. E. Casey and E. J. Hoffman, "Quantitation in positron emission: A technique to reduce noise in accidental coincidence measurement and coincidence efficiency calibration," *J. Comput. Assist. Tomogr.*, vol. 10, no. 5, pp. 845–850, 1986.

[36] B. E. Cooke, A. C. Evans, E. O. Fanthome, R. Alaire, and A. M. Sendy, "Performance figure and images from the Therascan 3128 positron emission tomograph," *IEEE Trans. Nucl. Sci.*, vol. 31, no. 1, pp. 640–644, 2005.

[37] M. Mayer *et al.*, "Performance of CdZnTe strip detectors as sub-millimeter resolution imaging gamma radiation spectrometers," in *Nucl. Sci. Symp. Conf. Rec.*, 1996, pp. 830–834.

[38] F. Zhang, Z. He, D. Xu, and L. J. Meng, "Feasibility study of using two 3-D position sensitivt CZT detectors for small animal PET," in *Nucl. Sci. Symp. Conf. Rec.*, 2005, pp. 4–8.

[39] Y. Yin, S. Komarov, H. Wu, Y. Y. Song, L. Qiang, A. Garson, K. Lee, G. Simburger, P. Dowkontt, H. Krawcyynski, and Y.-C. Tai, "Characterization of highly pixilated CZT detectors for sub-millimeter PET," in *Nucl. Sci. Symp. Conf. Rec.*, 2009, pp. 2411–2414.

[40] S. Grootoonik, T. J. Spinks, C. Michel, and T. Jones, "Correction for scatter using dual energy window technique in a tomography operated without septa," in *IEEE Nuc. Sci. Symp. Conf. Rec.*, 1991, vol. 3, pp. 1569–1573.

[41] J. M. Ollinger, "Model-based scatter correction for fully 3-D PET," *Phys. Med. Biol.*, vol. 41, pp. 153–176, 1995.